Metals & corrosion

Experimental and computational investigation of Ti-Nb-Fe-Zr alloys with limited Fe contents for biomedical applications

Camilo A. F. Salvador[1,*] , Mariana R. Dal Bo[2], Dalton D. Lima[2], Caetano R. Miranda[1], and Rubens Caram[2]

[1] Institute of Physics, University of Sao Paulo (USP), Sao Paulo, SP 05508-090, Brazil
[2] School of Mechanical Engineering, University of Campinas (UNICAMP), Campinas, SP 13083-860, Brazil

ABSTRACT

Among many β-metastable alloys explored for biomedical applications, alloys from the Ti-Nb-Fe-Zr system present great potential regarding cost and mechanical strength. In this article, we take a new look at the possibility of using Fe as a minor alloying element in the Ti-Nb-Fe-Zr system, with additions up to 2.0 wt% Fe. Additional compositions fixing the Nb/Fe ratio and changing Zr content from 7–13 wt% were also explored, resulting in a total of five different alloys. The samples were solution-treated and then subjected to three different conditions: water-quenched, furnace-cooled, and step-quenched to 450 °C for 12 h. Resultant microstructures were analyzed using X-ray diffraction, differential scanning calorimetry, scanning, and transmission electron microscopy. DSC experiments indicate that Zr might alter the phase transformations that occur during heating and cooling cycles. First-principles calculations confirmed that Zr's addition is crucial to reduce the elastic modulus of the β matrix and increase the ω-phase formation energy relative to β. All alloys presented mechanical properties suitable for biomedical applications; however, Ti-23Nb-2.0Fe-10Zr (wt %) stands out with the best combination of mechanical strength and elastic modulus after aging.

GRAPHICAL ABSTRACT
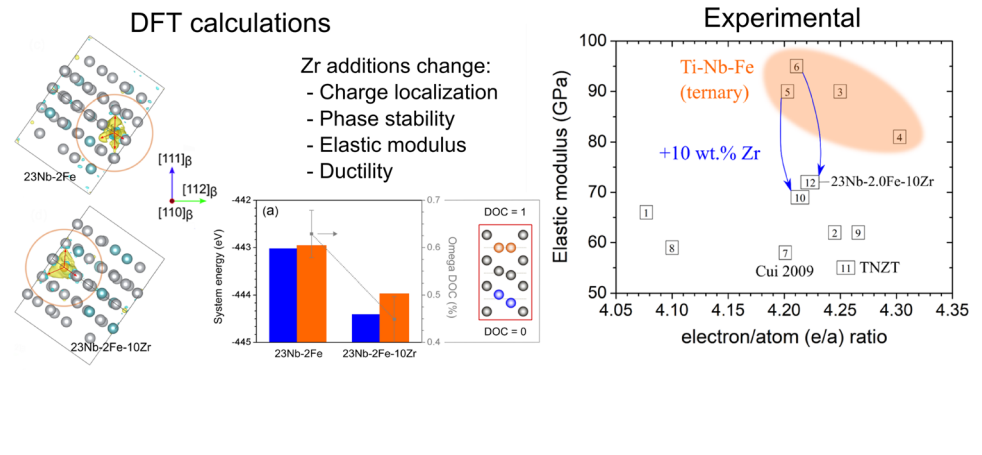
Introduction

Throughout recent history, Ti alloys have become unique materials for a wide range of applications in the chemical, aerospace, and biomedical industries owing to a combination of high-strength, low-density, and exceptional corrosion resistance. As a convention, titanium alloys can be divided into three different broad classes, designated as α, α + β, and β alloys. Nowadays, β and β-metastable Ti alloys are the preferred candidates in the field of orthopedic implants, thanks to their relatively low elastic modulus, biocompatibility, and an improved cold-workability compared to α-β alloys, due to a higher number of slip systems available in the bcc-β in comparison with the hcp-α crystal structure [1]. The number of studies concerning β-metastable Ti alloys has been growing consistently since the 1990s. The total number of publications indexed from Web of Science reached approximately one thousand four hundred fifty (1450) as of January 2021. It might rise in the following decades with further advances in alloy development, characterization techniques, and computational tools [2].

While some research has been carried out on Ti-Fe-based alloys, there is very little scientific understanding of Fe's role on the phase transformations in multicomponent Ti alloys. Since the early 1960s, studies with alloys containing more than 2.5 wt% Fe were discouraged. During the ingot fabrication, Fe's addition in high quantities led to its segregation to

regions called β-flecks, which were detrimental to mechanical performance [3]. Furthermore, the metallurgy community raised some concerns about the formation of the Ti-Fe intermetallic compound over a broad range of Fe additions in the Ti-Fe binary system. However, later works by Franti et al. and Lee et al. showed that in hypoeutectoid alloys such as Ti-5Fe (wt %), the formation of Ti-Fe occurred very slowly. According to the authors, the delay between the onset of proeutectoid α formation and the beginning of the bainite reaction—which in turn would produce Ti-Fe—is of the order of weeks, even at elevated soaking temperatures, slightly below the eutectoid temperature. Ti-Fe intermetallics could only be seen in Ti-5Fe after 28 days spent at 550 °C. When detected, the formation of Ti-Fe seemed to occur at impinged proeutectoid α-plates [4, 5]. Accordingly, these results opened the possibility to explore ternary systems with Fe further. As an example, the design of Ti-Mo-Fe and Ti-Mo-Fe-Zr in the early 2000s paved the way to design new alloys with low cost and high mechanical strength [6, 7].

On the other hand, only a few papers had been published exploring the Ti-Nb-Fe system in 15 years. Most of them analyzed either as-cast samples of binary Ti-Nb alloys, with diversified additions of Fe, or solution-treated samples subjected to water quenching or continuous cooling [8, 9]. As an example, Lopes et al. (2016) showed that additions of 1–5 wt% Fe to Ti-30Nb alloys could induce significant strength improvements relative to the Ti-Nb binary system [10]. In 2009, Cui & Guo designed a novel

alloy named TNZF (Ti-28Nb-13Zr-0.5Fe wt%). Forged samples subjected to ST-WQ presented yield strength of 800 MPa, elongation of 13%, and an elastic modulus of 60 GPa. The microstructure was composed of primary β-grains and a small volumetric fraction of α". After aging at 450 °C for four hours, the precipitation of ω and α-phases led to increased yield strength and elastic modulus to 950 MPa and 80 GPa, respectively [11]. A few papers revisited the Ti-Nb-Fe-Zr system during the last years, showing how promising this system could be [12–14]. The possibility of using Fe as an alloying element has also regained interest in the past years due to the consolidation of new processing routes based on additive manufacturing using low-cost TiH_2 powder feedstock. In this case, Fe enhances the sinterability of AM pieces thanks to its high diffusivity in Ti, significantly accelerating the initial sintering stage [15]. This article takes a new look at the possibility of using Fe as a minor alloying element (i.e., with additions below 2.5 wt%) in a quaternary system alongside Nb and Zr. Zr was selected as an ω-suppressor element because its addition can increase the energy barrier to ω-formation relative to other systems without this element [16].

In this paper, we analyzed a total of five compositions; three of them are obtained by fixing the Zr weight fraction and varying the Nb/Fe ratio—Ti-23Nb-2.0Fe-10Zr, Ti-27Nb-1.5Fe-10Zr, and Ti-31Nb-1.0Fe-10Zr (wt %). Two additional compositions are prepared by varying the Zr content from 10 to 7 or 13 wt%, e.g., Ti-27Nb-1.5Fe-7Zr, Ti-27Nb-1.5Fe-13Zr. Thus, Nb/Fe (atomic) ratios explored were 6.9 (Ti-23Nb-2.0Fe), 10.8 (Ti-27Nb-1.5Fe), and 18.6 (Ti-31Nb-1.0Fe). The alloys were designed hoping that high Nb/Fe ratios could present a reduced elastic modulus with respect to the compositions previously reported in Dal Bo et al. [14]. Computational and experimental data gathered during this work evidence the chosen compositions are promising candidates to the biomedical field, presenting a relatively high elastic admissible strain (EAS, i.e., the yield strength to elastic modulus ratio).

Materials and methods

Experimental

The five alloys investigated in this study were prepared via arc-melting under an argon atmosphere. For this purpose, we used an electric-arc furnace with a non-consumable tungsten electrode and a water-cooled copper crucible. High-purity (> 99.95 wt %) precursor metals were employed. The 70 g ingots were flipped and re-melted six times to ensure chemical homogeneity. Afterward, ingots were encapsulated in quartz tubes with argon and subjected to a homogenization heat-treatment at 1000 °C for 12 h, followed by water-quenching by breaking the quartz tubes. The ingots were cold-rolled to 20% of their original thickness and then subjected to a solution/recrystallization heat-treatment at 800 °C for 10 min, followed by either (i) water-quenching (WQ), (ii) furnace cooling (FC), or (iii) step-quenching (SQ) to 450 °C for 12 h. The cold-rolling step was necessary to obtain a specific thickness and ensure a smaller grain size after recrystallization. The step-quenching aging process (iii) was selected to mitigate iso-ω (isothermal omega) formation, and consists of solution heat-treatment immediately followed by holding the samples at the desired temperature, in this case, 450 °C. This treatment was performed with two independent hot-zones and followed by water-quenching.

The ST-WQ samples' composition was confirmed by X-ray fluorescence technique (XRF) using a Shimadzu EDX7000 equipment. The interstitial O and N contents were analyzed via the inert gas fusion method (LECO TC400). The chemical composition of the experimental alloys is displayed in Table 1.

Vickers hardness measurements were obtained with a Buehler Vickers 2100 hardness tester, applying an indentation load of 1 kgf load applied for 15 s. Elastic modulus measurements of the 2 mm thick samples were taken using a pulse-echo Panametrics NDT 5072PR emitter–receiver equipped with 7.5 mm round transducers operating at a frequency of 5 MHz. WQ samples later subjected to aging at 350 °C for 24 h were analyzed via DSC measurements using a NETZSCH STA 409 C purged with argon. Heating and cooling rates were set to 25 K/min, over a temperature range from RT to 800 °C, to detect the ω-solvus temperature. The samples for the DSC experiments weighted 70 mg, on average.

Table 1 Composition of the five experimental alloys (wt %); Ti in balance

Alloy (wt. %)	Nb	Fe	Zr	O	N	e/a
Ti-23Nb-2.0Fe-10Zr	22.2 ± 0.6	2.3 ± 0.2	9.9 ± 0.3	0.186 ± 0.002	0.006 ± 0.002	4.22
Ti-27Nb-1.5Fe-7Zr	24.8 ± 0.4	1.7 ± 0,2	7.1 ± 0.2	*	*	4.23
Ti-27Nb-1.5Fe-10Zr	26.1 ± 0.3	1.5 ± 0.1	10.1 ± 0.1	0.140 ± 0.009	0.014 ± 0.004	4.23
Ti-27Nb-1.5Fe-13Zr	25.4 ± 0.3	1.6 ± 0.1	13.1 ± 0.1	*	*	4.24
Ti-31Nb-1.0Fe-10Zr	29.7 ± 0.8	1.3 ± 0.2	10.2 ± 0.2	0.131 ± 0.002	0.008 ± 0.002	4.24

*Interstitials were determined to the alloys subjected to tensile tests only

Samples were subjected to a conventional metallographic preparation. Kroll's reagent (6 mL of HNO_3, 3 mL of HF, and 91 mL of H_2O) was used for metallographic etching of the samples analyzed via visible-light microscopy (Olympus BX60M). Scanning electron microscopy (SEM) images were acquired using a ZEISS EVO MA15 scanning electron microscope operating at 20 kV. Transmission electron microscopy (TEM) images were obtained with the aid of a JEOL 2100 (200 kV, LaB6 source) from conventional 3 mm disks prepared via mechanical punching, grinding, and polishing. The disks were subjected to argon ion milling at ∼ 4 kV and an incident angle of ± 6°, while in contact with a holder cooled with liquid N_2.

Cylindrical, hot-swaged samples were prepared exclusively for the tensile tests. Ingots were heated up 1000 °C and then hot-swaged with a reduction of approx. 3 mm in diameter each step (four to five forging steps total), down to 9 mm. Cylindrical tensile specimens with 4 mm of diameter and 26 mm of gauge length were then milled from the bars and subjected to the desired heat-treatment. Fixation at the universal testing machine was done at both edges by M8 threads.

DFT calculations

First-principles calculations based on the density functional theory (DFT), as implemented in the Vienna Ab-initio Simulation Package (VASP) [17], were carried out to investigate the energetic and elastic properties of specific alloys derived from Ti-23Nb-2.0Fe-10Zr (wt.%). The projector-augmented wave (PAW) method with the corresponding PAW pseudopotentials and PBE functional were employed. The energy cutoff was set to 400 eV. The Brillouin zone was sampled by an equivalent of 27 k-points in the bcc primitive cell. Special-quasi-random-structures (SQSs) with 54 atoms were built with

the aid of the ATAT package [18] to model each composition. The configuration of each cell was Ti46-Nb8 and Ti-43-Nb8-Zr3 (at.%) corresponding to approx. Ti-23Nb-2.0Fe and Ti-23Nb-2.0Fe-10Zr (wt.%), respectively. They were relaxed until forces smaller than 0.02 eV/Å were reached. Elastic constants were obtained from the second derivative of the internal energy with respect to orthorhombic and monoclinic strain tensors, as described in Pezold et al. [19]; the deformations were applied to the relaxed β-phase cells, in four deformation steps, maxing out 2% strain. Two-dimensional projections of the bulk modulus (K), shear modulus (G), and Poisson's ratio were generated in the ELATE suite, developed by Gaillac et al. [20].

Charge density differences were computed by self-consistent calculations with a fine k-point grid (the equivalent of 54 k-points in the primitive cell); they were calculated to identify the charge rearrangement due to the presence of Fe atoms in the β-phase. One reference structure was computed for each alloy since atomic positions are different due to ionic relaxation. The charge density differences associated with Fe additions ($\Delta\rho$, in e/Å3) are assumed to be:

$$\Delta\rho = \rho_s - (\rho_{srFe} + \rho_{atFe}) \qquad (1)$$

where $\rho_s, \rho_{srFe}, \rho_{atFe}$ are the total charge density of the converged structure, of the converged structure removing the Fe atom, and an isolated Fe atom at the same atomic site, respectively. Charge density files were post-processed with VESTA [21].

Alloy design

In Ti alloys, the valence electrons per atom ratio (e/a) can significantly influence the elastic modulus. Experiments with the Ti-Nb and Ti-V binary alloys have shown that a minimum modulus can be obtained in these systems with an e/a ratio between 4.24 and 4.26 [22]. According to Saito et al., in this

range, the difference between the elastic components C11 and C22 is small, which implies the single-crystal Young's modulus in the < 001 > direction, and the shear modulus along < 111 > {011}, {112} and {123} slip systems must be small. In this way, the elastic modulus should be minimized [23]. As shown in Table 1, the alloys' e/a ratio is close to the reported optimal range. However, it goes down to 4.22 (Ti-23Nb-2.0Fe-10Zr) as we substituted Nb with Fe. The relationship between the e/a ratio and the resultant elastic modulus will be discussed in the results section. In regard to Zr, since Zr partially substitutes Ti atoms in the lattice, significant alterations in the e/a ratio are not expected. As stated before, the benefits of using Zr are associated with its ω-phase suppressing abilities.

In addition to essential aspects of alloy design already covered in the introduction, another attractive property of our alloys is hardenability. According to Cotton et al. 2015, hardenability is the ability to produce a functional metastable condition in the β-phase during quench, with a significant age-hardening response from the supersaturated β-phase during aging [24]. In the proposed alloys, the high quantity of β stabilizers (Nb + Fe) helps avoid an extensive formation of martensite or ω-phase. Furthermore, the high Nb/Fe ratio hinders the formation of diffusion-controlled α-phase, since Nb is a slow diffuser in Ti. Small additions of Fe are still there to act as fast diffusers, allowing controlled precipitation of α-phase during aging [25].

Results and discussion

Preliminary tests with Ti-27Nb-1.5Fe-xZr

To establish a reference frame, we started analyzing samples subjected to ST-WQ and ST-FC, which could easily be compared to their parents from the ternary system [26]. It is worth reminding that the presence of (athermal) ath-ω also causes significant alterations in the Vickers hardness, beyond changing the elastic modulus [27, 28]. Vickers hardness for Ti-27Nb-1.5Fe with Zr additions is shown in Fig. 1. Zr additions can significantly reduce Vickers hardness in comparison with the base alloy. It seems the reduction reaches a threshold with additions between 10 and 13 wt% of Zr. In the ST-WQ condition, an elastic modulus close to 65 GPa was obtained for Ti-27Nb-1.5Fe with additions of 10 and 13 Zr (wt%). These results can be considered promising in comparison with other compositions with much higher Zr contents, such as Ti-25Nb-41Zr [29]. Concerning the FC samples, the addition of Zr to the Ti-Nb-Fe system has led to interesting divergences, compared to the base system. For Ti-27Nb-1.5Fe, a significant drop in hardness and elastic modulus is observed with the Zr addition. It can be inferred that the Zr additions help to suppress the isothermal omega (iso-ω) phase previously formed in Ti-27Nb-1.5Fe (ternary) upon FC.

The initial idea behind the Zr addition was to partially suppress the omega (ω) phase formation by a structural destabilization. XRD analyses were performed for all the experimental alloys after WQ or FC and are presented in Fig. 2. As the microstructure has phases with a limited size, the analysis of conventional XRD data must be performed with caution. For the ST-WQ samples, Zr's addition seems to efficiently

Figure 1 Hardness and elastic modulus as a function of the Zr content for Ti-27Nb-1.5Fe-xZr. Data from WQ samples are displayed in black; FC samples in blue.
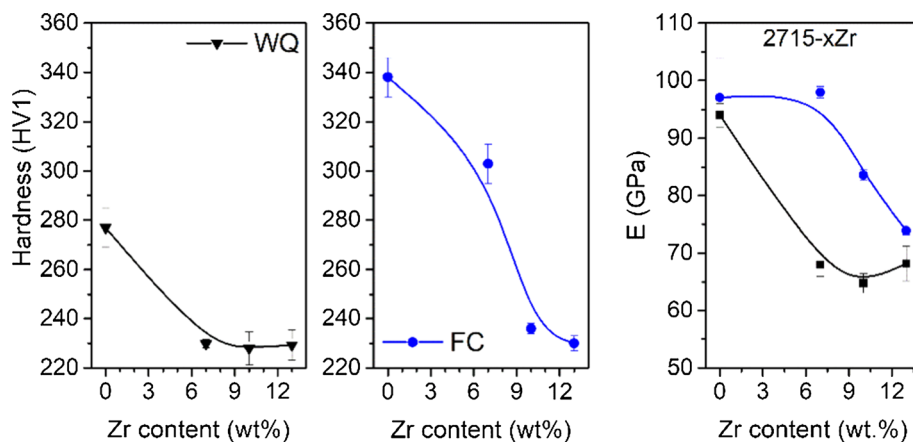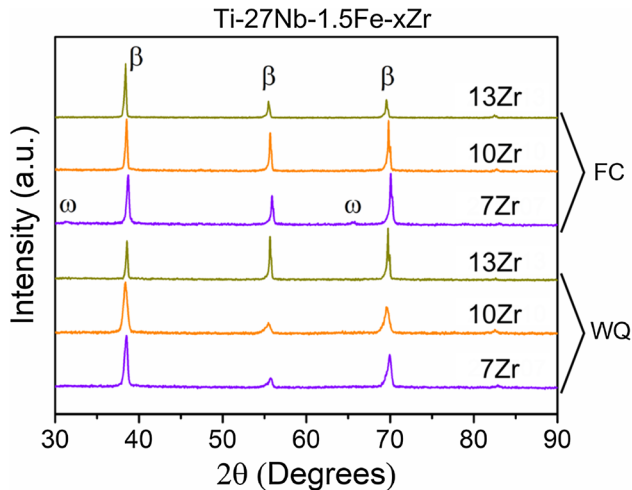
Figure 2 X-ray diffraction of the ST-WQ (below) and ST-FC samples. Compositions are abbreviated as follows: Ti-27Nb-1.5Fe-10Zr = 271,510.

hinder the formation of the ath-ω, since no ω could be detected via XRD. During cold rolling, we noticed a moderate improvement in the cold formability with the quaternary alloys. Omega-phase was not detected in Ti-27Nb-1.5Fe-10Zr samples after ST-WQ (Fig. 3) via TEM either. According to the literature, the addition of 5–7 wt% of Zr to Ti-Mo-Fe alloys is enough to suppress the formation of ath-ω upon water-quenching [30, 31], which corroborates with our results.

On the other hand, in the FC condition, ω-phase peaks are seen in the diffractograms from Ti-27Nb-1.5Fe-7Zr, probably due to the slow cooling process that enables the formation of isothermal ω-phase. The results obtained in this work pointed to the necessity of slightly higher Zr additions (10 wt%) to Ti-Nb-Fe alloys to avoid the formation of isothermal ω-phase

during cooling. Additionally, the broadening of β peaks near $2\theta = 70$ degrees could suggest the appearance of either α or martensitic phases (α′ and α″) in these samples. However, this is unlikely to be the case since no other peaks were detected. Furthermore, in these alloys, the quantity of β stabilizers is sufficient to depress the martensite start (Ms) associated with α′ and α″ to below room temperature [32, 33]. Conversely, Nb contents should limit α-phase formation and growth due to its limited diffusion in the β matrix [34].

As a preliminary analysis, DSC scans were performed for Ti-27Nb-1.5Fe-10Zr (the intermediate composition concerning the Nb/Fe ratio). As previously described in Costa et al. 2016 and Salvador et al. 2017, samples were subjected to aging at 350 °C for 24 h to produce microstructures with well-developed iso-ω-phase precipitation before the scans. With an elevated ω-phase volumetric fraction, the phase-transformation events could be easily detected [25, 26].

DSC thermograms are presented in Fig. 4. The image displays peaks associated with the iso-ω formation and decomposition. However, they are less energetic relative to ones detected in the ternary system [26]. This behavior might be associated with the Zr presence in the alloy since Zr reduced the iso-ω volumetric fraction obtained after aging relative to the ternary system. On the other hand, the exothermic peak associated with α-phase is very subtle and can only be highlighted in the first heating cycle (450 °C < T < 500 °C). Based on previous results from the ternary system, Zr may cause the reduction of ω-solvus temperature, enabling α-phase to form at lower temperatures among the quaternary alloys.

Figure 3 Bright-field of the Ti-27Nb-1.5Fe-10Zr TEM sample (ST-WQ) and its respective selective-area electron diffraction (SAED). Images recorded through the [102]β zone axis. Only β-phase was detected.
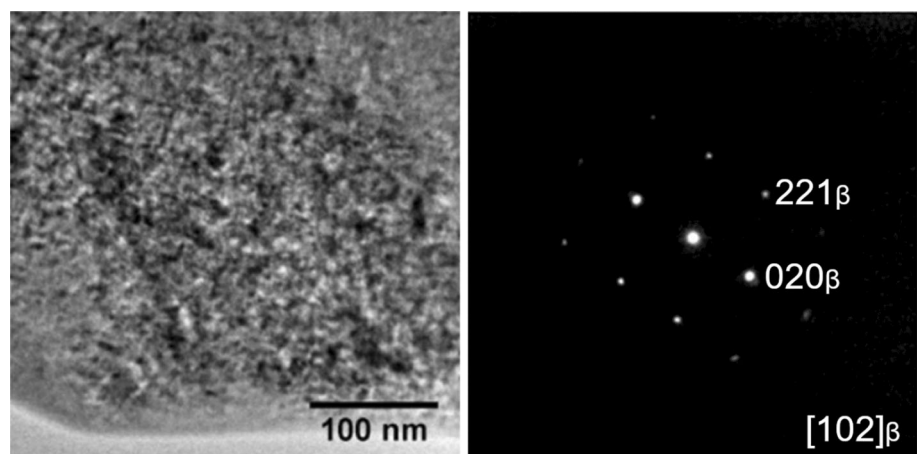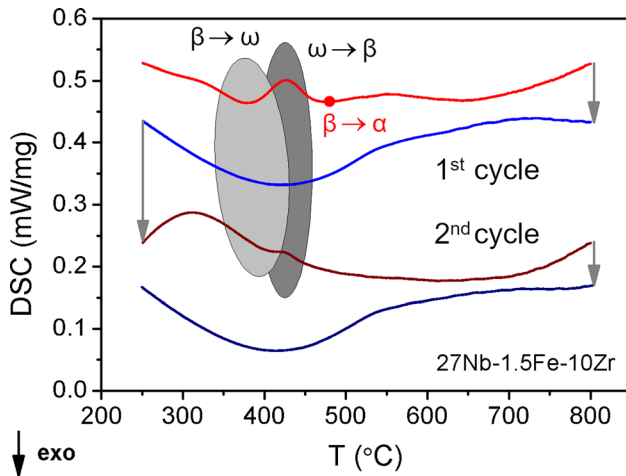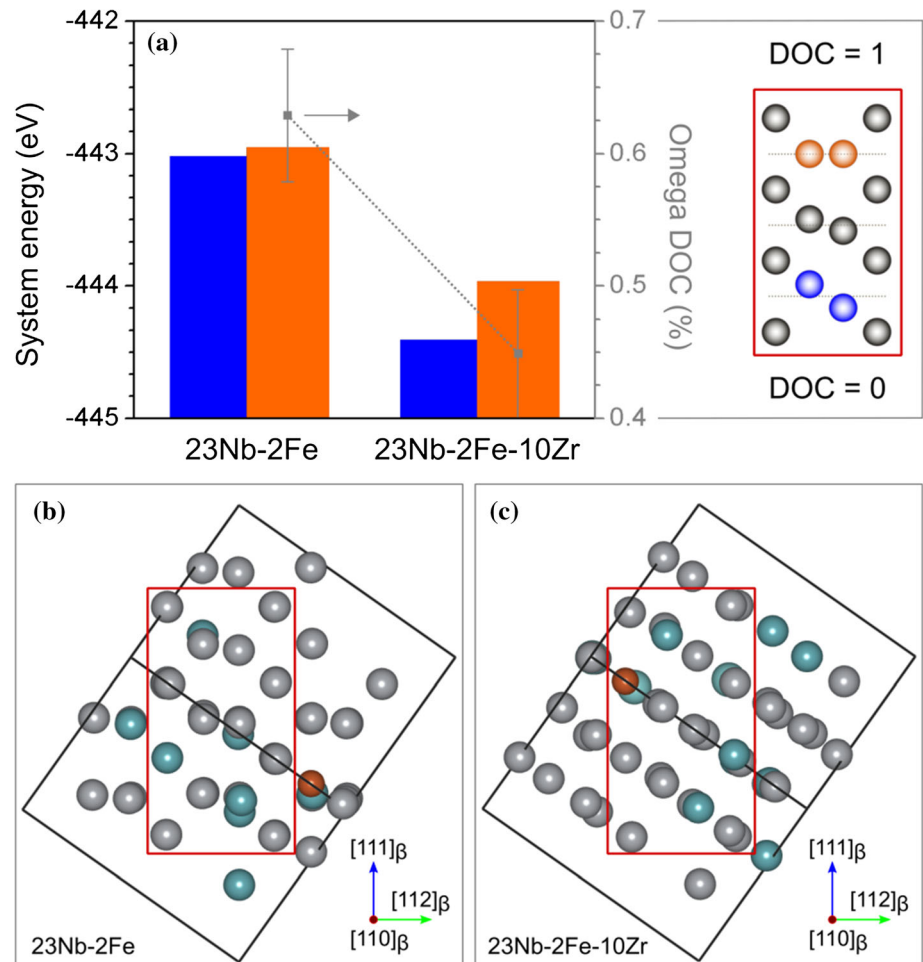
Figure 4 DSC curves (2 consecutive cycles) recorded for Ti-27Nb-1.5Fe-10Zr. The formation and dissolution of ω are followed by the formation of alpha near 450 °C. Red tones represent heating cycles, and blue tones cooling cycles, respectively.

Computational investigation

DFT analysis of the ω-phase

To evaluate the ω-phase stability via DFT, we take the ω-structures after relaxation and compare it to the prior β-structure. A degree of collapse (DOC) of 1 means the atoms that collapsed to form ω are still at the same positions expected for a standard ω crystal structure. On the other hand, a DOC = 0 means the ω structure fully relaxed into β; therefore, the atoms returned to their original positions before the collapse [35, 36]. In Fig. 5, one can see that the energies of β and ω phases are much closer in the Ti-23Nb-2.0Fe (b) alloy supercells. Also, the degree of collapse of ω after relaxation is 63%, which is relatively close to an ideal ω crystal structure (DOC = 1). On the other hand, in the Ti-23Nb-2.0Fe-10Zr cell (c), the ω-phase relaxed into a partially-collapsed ω, with the centered atoms positioned almost at the bcc primitive positions. Following this behavior, the β-phase has

Figure 5 Energy of the 54 atom supercells after relaxation; initial structures set to β-phase (blue) and ω-phase (orange) phases for each composition; the degree of collapse after relaxation is shown in gray (right-hand axis), next to an illustration that shows DOC = 0 and DOC = 1; **b** depicts the ω-phase cell for Ti-23Nb-2.0Fe after relaxation and (**c**) illustrates the same for Ti-23Nb-2.0Fe-10Zr. Note that (**c**) is very similar to a bcc structure.

relatively lower energy than ω in this case, and the estimated DOC is small after relaxation (DOC = 43%). It is worth reminding that a DOC = 0 equals a perfect β crystal structure. In other words, DFT calculations pointed to a destabilization of ω in the Zr presence, favoring a bcc-like phase formation upon quench. These results support previous statements and data collected via DSC.

DFT analysis of the β-phase

An in-depth analysis of the β-phase structures after relaxation adds interesting data to the problem in-hand. By analyzing Fe atoms' neighborhood, it is intriguing to note significant atomic displacements towards the Fe atom, causing lattice distortions in both compositions (Fig. 6). However, while in Ti-23Nb-2.0Fe the bond distortions follow a bimodal distribution, with a few bonds parallel to the [111]β direction being severely affected (Fig. 6a), the local bond distortions in the presence of Zr are more homogenous (Fig. 6b). We believe these atomic configurations result from the electronic charge density distributions (Δρ) around the Fe atoms in each alloy.

In general, positive Δρ are localized along with Ti-Fe bonds, favoring such bonds. In Ti-23Nb-2.0Fe, electron-excess and depletion zones are found alongside the [111]β direction, increasing directional stiffness and most likely favoring the collapse of β to form this ω-variant (Fig. 6c). As can be observed in Fig. 6d, an opposite behavior is seen in Ti-23Nb-2.0Fe-10Zr, which presents delocalized Δρ that decrease the bonds' overall covalent character and promote an elastic softening of the structure. Local distortions and charge distributions corroborate with Ti alloys' phase stability and mechanical behavior, as discussed by Choudhuri et al. [35]. In the absence of Zr, depletion zones generated by Fe cause large local atomic distortions, induce the ω-phase formation and result in increased elastic stiffness. Fortunately, Zr additions can change the charge density distribution around Fe, promoting charge delocalization and balanced atomic displacements, contributing to higher β-phase stability.

Finally, the elastic properties of Ti-23Nb-2.0Fe with and without Zr additions are illustrated in Fig. 7. Figure 7c–f also shows a marginal increase in the Poisson-ratio anisotropy (1.20 vs. 1.08) with the Zr

Figure 6 Bond distortions around Fe atoms for Ti-23Nb-2.0Fe (**a**) an Ti-23Nb-2.0Fe-10Zr (**b**). Figures (**c**) and (**d**) display the electron charge difference plots associated with the Fe atom in each alloy. Charge density differences (Δρ) created with VESTA [21] are displayed in yellow with 0.05 e/Å³ iso-charge surfaces. Depletion zones are presented in blue. Atoms were colored with a standard CPK coloring scheme. Red arrows indicate increasing stiffness vectors.
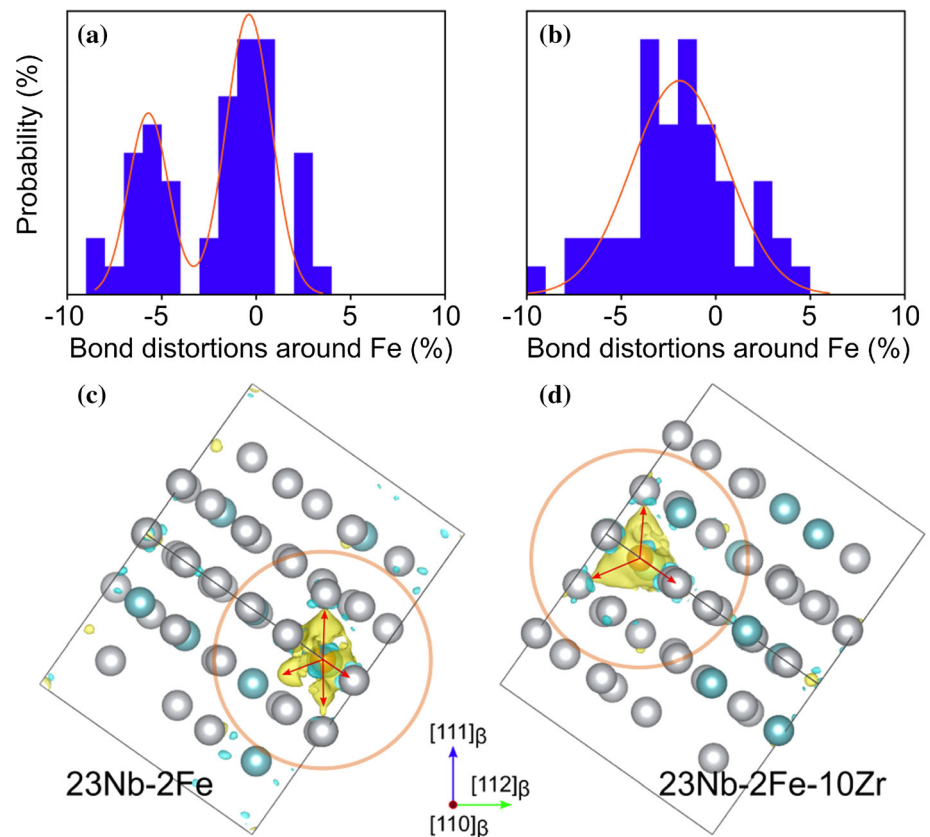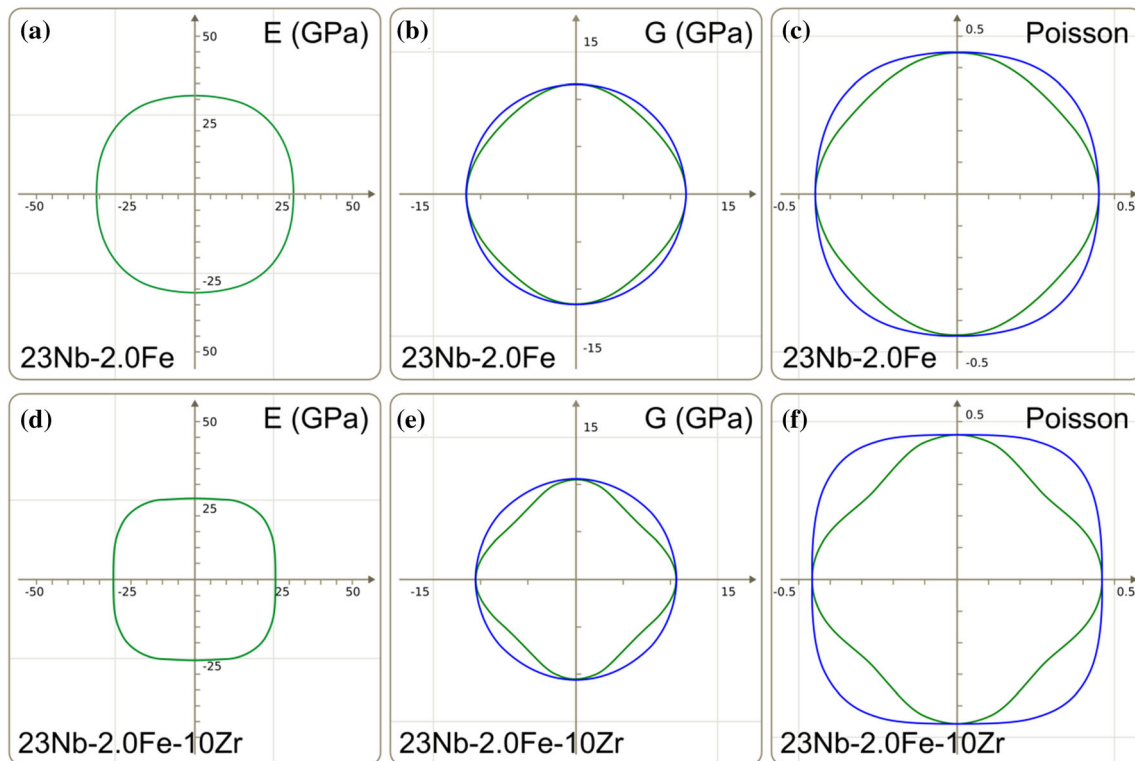
Figure 7 2D projections of the elastic modulus, shear modulus, and Poisson's ratio for each cell obtained via DFT. Maximum values are shown in blue and minimum in green.

Table 2 Elastic constants obtained via DFT.

Alloy (wt. %)	K (GPa)	C_{11}	C_{12}	C_{44}	Poisson	Poisson anis
Ti-23Nb-2.0Fe	110.0	124.3	102.9	11.6	0.45	1.08
Ti-23Nb-2.0Fe-10Zr	104.9	116.7	99.0	10.6	0.45	1.20

The bulk modulus is referred to as K

addition. The difference between the elastic components C_{11} and C_{22} was not significantly affected. In absolute values (Table 2), the elastic modulus of the β-phase (Voigt–Reuss–Hill averages) could be reduced by roughly 13% with the addition of Zr (Table 2). However, this reduction does not take into account the energy minimization of β, which hinders the formation of ω. In other words, the addition of Zr to Ti-23Nb-2Fe has two direct benefits: it reduces the elastic modulus of the β matrix and also increases the ω-phase formation energy relative to β, ultimately suppressing ω formation.

Experimental verification

Now that all theoretical implications concerning Fe and Zr solutes were exposed let's turn our attention to experiments performed with samples with varied Nb/Fe ratios and Zr content fixed to 10 wt%. X-ray diffraction patterns of such samples are presented in Fig. 8. One more time, WQ samples presented a full β-structure. According to the TEM analysis shown in Fig. 3 and in Dal Bo et al. [14], the addition of 10 wt% of Zr to the ternary alloys Ti-19Nb-2.5Fe and Ti-27Nb-1.5Fe thoroughly suppresses ath-ω-phase formation upon quenching. The same is expected for Ti-23Nb-2.0 Fe based on the DFT predictions presented in Fig. 5. As Ti-31Nb-1.0Fe also has considerable amounts of Nb, it could be inferred that ω-ath would also be suppressed upon the same addition.

Figure 8b shows the diffractograms obtained from samples subjected to solution treatment followed by a step-quench to 450 °C for 12 h. The diffractograms

Figure 8 XRD data on the (**a**) ST-WQ and (**b**) aged conditions. Samples with Zr content fixed to 10 wt.%.
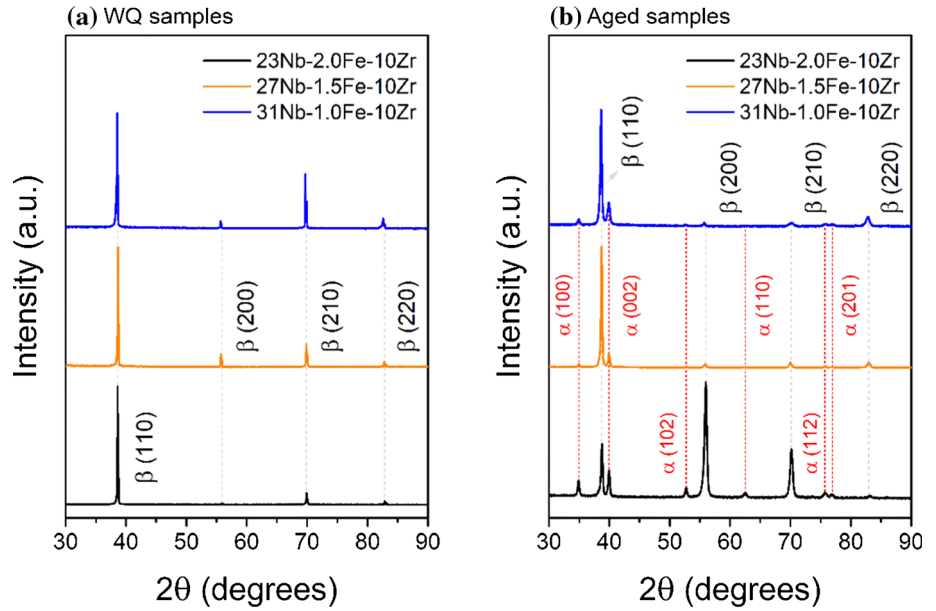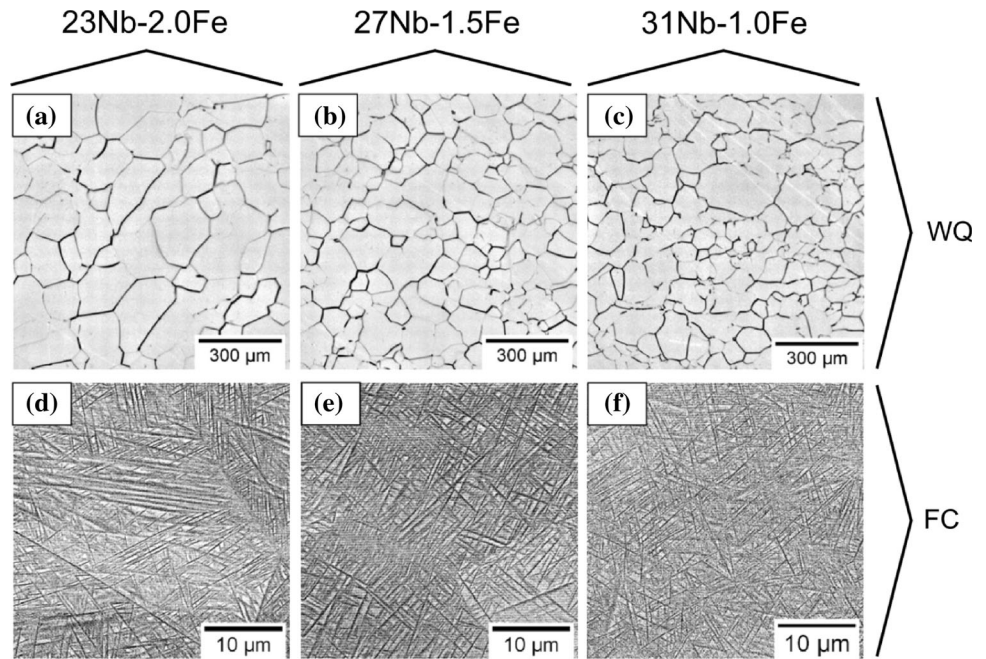

Figure 9 Optical micrographs of the WQ samples (**a**–**c**) and SEM of the aged samples (**d**–**f**). All compositions with 10 wt.% of Zr. As labeled, images are related to Ti-23Nb-2.0Fe-10Zr, Ti-27Nb-1.5Fe-10Zr and Ti-31Nb-1.0Fe-10Zr from left to right, respectively. This image refers to cylindrical, hot-swaged specimens.

point to a successful strategy in getting fine and dispersed α-precipitates through the β matrix without detectable ω-phase formation. The temperature of 450 °C—which is above ω-*solvus* for Ti-27Nb-1.5Fe-10Zr and therefore for all experimental alloys—was chosen based on the previous DSC results presented in Fig. 4. The microstructures of the WQ and aged samples are further detailed in Fig. 9. As shown in the optical micrographs presented in Fig. 9a–c, WQ samples present only β grains, with a broad size distribution, due to the mechanical processing and

fast recrystallization performed before the characterization. It appears Ti-23Nb-2.0Fe-10Zr has an average grain size greater than the others, and this could be associated with either the composition or the thermomechanical processing; however, this particular analysis was not addressed in the present work. The reader should be aware that the smaller grains could result in an overestimation of yield strengths in Ti-27Nb-1.5Fe and Ti-31Nb-1.0Fe based alloys due to the well-known Hall–Petch relationship [37]. As for the aged samples (Fig. 9d–f), one can observe fine and

dispersed α-phase, without much development of the precipitates at the grain boundaries, which is beneficial to ductility. As the images were recorded with a backscattered electrons (BSE) detector's aid, it can be inferred that Nb has been concentrated in the β-phase (brighter), as expected for such long heat-treatments. Nb-rich regions appear brighter in BSE images since they scatter more electrons, given Nb's superior atomic number.

Tensile tests presented at the WQ and aged conditions are presented in Fig. 10a and b, respectively. As expected, the lower Nb/Fe ratio (higher Fe content) in Ti-23Nb-2.0Fe-10Zr led to overall higher yield strengths, given that Fe has an essential role in solid-solution strengthening of the β-phase [38]. On the other hand, high Nb contents led to improved ductility. Ti-31Nb-1.0Fe-10Zr reached an average elongation at failure of 15 ± 6%, the higher strain among the experimental alloys.

Concerning the heat-treated specimens, Ti-23Nb-2.0Fe-10Zr performed best in response to aging, with an average yield strength of 980 ± 62 MPa. In Ti alloys, the β/α interfaces block the dislocation motion; hence, the mechanical strength of any β + α microstructure derives mainly from the size, morphology, and distribution of the α phase. Usually, the finer the α-phase size distribution, the higher the resultant mechanical strength. An interesting point to be noted in the mechanical tests (Fig. 10b) is that although the α-phase size distribution in Ti-31Nb-1.0Fe-10Zr (Fig. 9f) appears more refined than in Ti-23Nb-2.0Fe-10Zr (Fig. 8d), the Fe-rich alloy presented a higher yield strength, which is controversial.

Therefore, in this case, it seems the solid-solution reinforcement of Fe within the β-matrix is dominant over the size of the α-phase laths resultant from aging. In Fig. 10a, it is also possible to observe a non-uniform deformation before necking in Ti-27Nb-1.5Fe-10Zr, which could be associated with the composition.

A compilation of the mechanical properties obtained in this study is presented in Table 3. Despite the sound results reported in this section, none of the high-Nb alloys performed as well as the Ti-19Nb-2.5Fe-10Zr (1027 MPa, 69 GPa) with respect to the mechanical properties [14]. In other words, Ti-19Nb-2.5Fe-10Zr seems to present an optimal trade-off between mechanical strength and low elastic modulus, reaching a unique elastic admissible strain.

Based on the fractured surfaces presented in Fig. 11, a ductile rupture mechanism is evident among the WQ samples. The side view images (Fig. 11a–c) display a vast necking region for all specimens, with a familiar cup-and-cone shape [39]. Fractured surfaces are covered by dimples and a few opened-up pores (dark), which indicate a predominant ductile behavior. Dimpled rupture involves three stages: void nucleation, growth, and coalescence. According to Van Stone et al. (1978), in Ti alloys, void nucleation should occur on blocked slip-bands or deformation twins (in the absence of a second phase). Then, the voids propagate through twin boundaries or grain boundaries, taking advantage of the multiple deformation modes available on both sides of these boundaries [40], which agrees with our experimental observations. Most fractures seem to
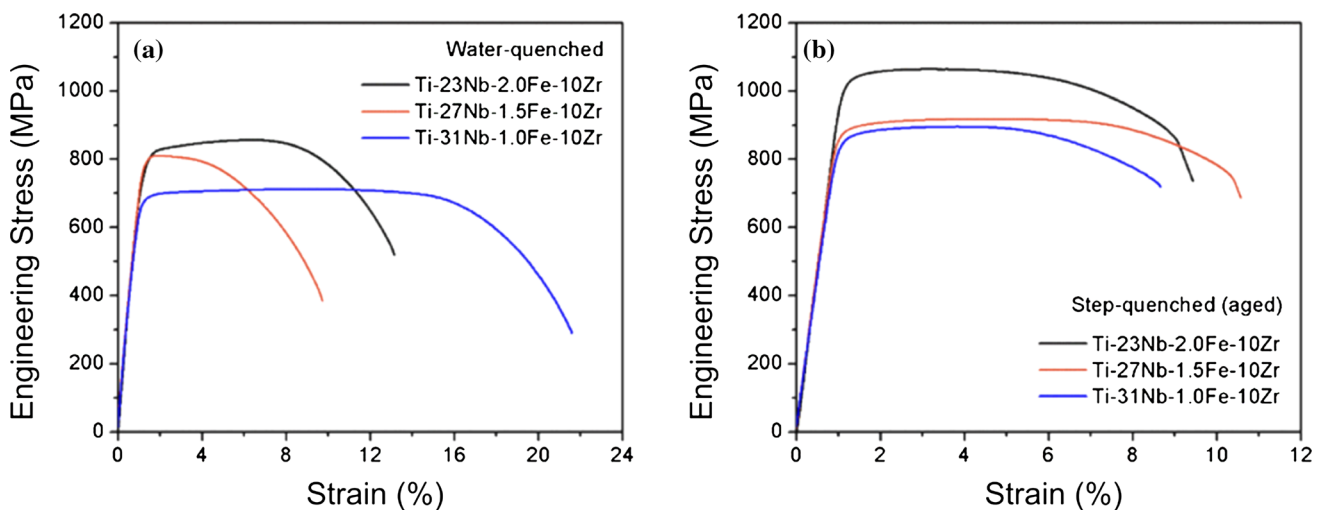

Figure 10 Stress–strain curves for the experimental alloys at the ST-WQ condition (a) and the aged condition (b).

Table 3 Compilation of the mechanical properties of high-Nb alloys

Alloy	Condition	Hardness (HV$_1$)	Yield strength (MPa)	Elastic modulus (GPa)	Elastic modulus (GPa)*	Elongation at break (%)
Ti-23Nb-2.0Fe-10Zr	WQ	252 ± 8	782 ± 62	79 ± 1	72 ± 2	10 ± 1
	Aged	316 ± 5	980 ± 62	104 ± 10	87 ± 2	8 ± 1
Ti-27Nb-1.5Fe-10Zr	WQ	229 ± 2	735 ± 94	78 ± 3	77 ± 2	9 ± 1
	Aged	301 ± 9	903 ± 33	101 ± 5	85 ± 3	8 ± 3
Ti-31Nb-1.0Fe-10Zr	WQ	218 ± 5	672 ± 99	77 ± 2	75 ± 2	15 ± 6
	Aged	278 ± 7	796 ± 94	89 ± 1	86 ± 4	10 ± 5

Two elastic modulus measurements, via tensile tests and the *pulse-echo technique

Figure 11 Fractography of the samples subjected to ST-WQ. Side view of the specimens after testing (**a**–**c**), overview (**d**–**f**), and detailed (**g**–**i**) SEM images of the fractured surfaces. From left to right, respectively: Ti-23Nb-2.0Fe-10Zr, Ti-27Nb-1.5Fe-10Zr and Ti-31Nb-1.0Fe-10Zr. This image refers to cylindrical, hot-swaged specimens.
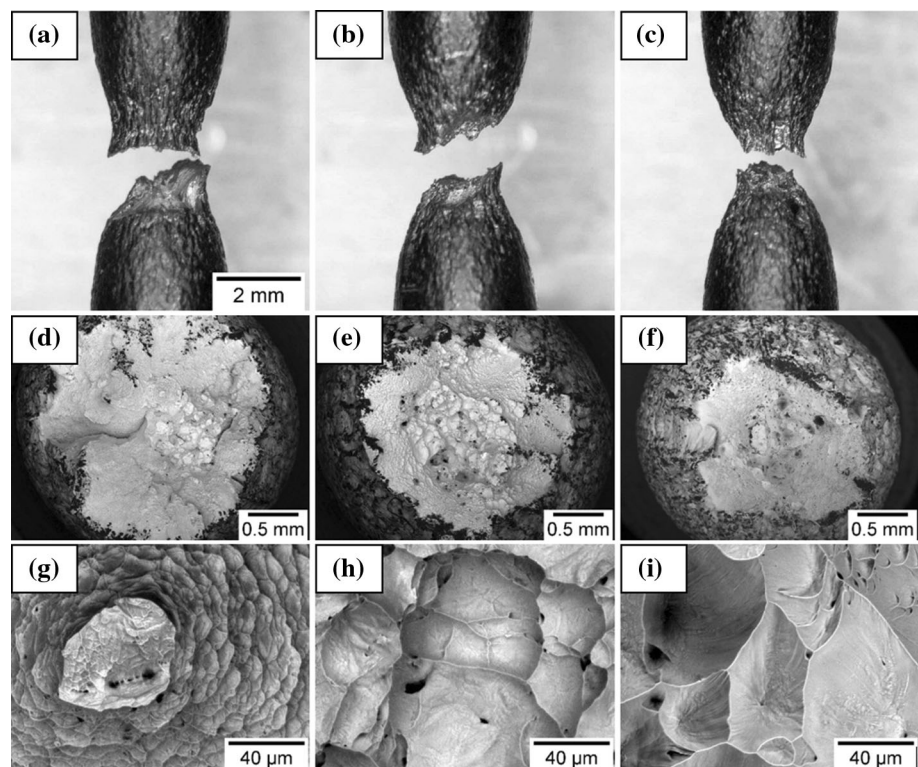
occur due to void coalescence. Furthermore, a higher Nb/Fe ratio appears to be associated with fewer dimples, elongated, and more generous in size in Ti-31Nb-1.0Fe-10Zr specimens. A difference in the density and size of dimples based on composition was also reported in Lopes et al. (2016) while exploring the Ti-Nb-Fe system, corroborating these observations.

As for the aged specimens, the side view (Fig. 12a–c) displays a mild necking and a few sharp ledges, which could be representative of both ductile and brittle (mixed) fracture modes. However, the fracture surfaces encompass a high density of varied sized dimples and opened-up pores, typical of ductile-dominant fracture. The micro-fracture images are also dominated by dimples, as can be seen in Figs. 12g–i. That makes sense since the average elongation at break for the aged specimens reaches 8%. As a frame of reference, heat-treated Ti-5553 presents a quasi-cleavage, transgranular fracture mode under tensile, with a predominance of cleavage facets over dimples. In the case of Ti-5553, elongation at break is often limited to 2% [41]. In this context, it could be stated that the alloys explored in this work still present a relatively high-ductility, even after being subjected to aging heat-treatments. On the

Figure 12 Fractography of the samples subjected to aging. Side view of the specimens after testing (**a**–**c**), overview (**d**–**f**), and detailed (**g**–**i**) SEM images of the fractured surfaces. From left to right, respectively: Ti-23Nb-2.0Fe-10Zr, Ti-27Nb-1.5Fe-10Zr and Ti-31Nb-1.0Fe-10Zr. This image refers to cylindrical, hot-swaged specimens.
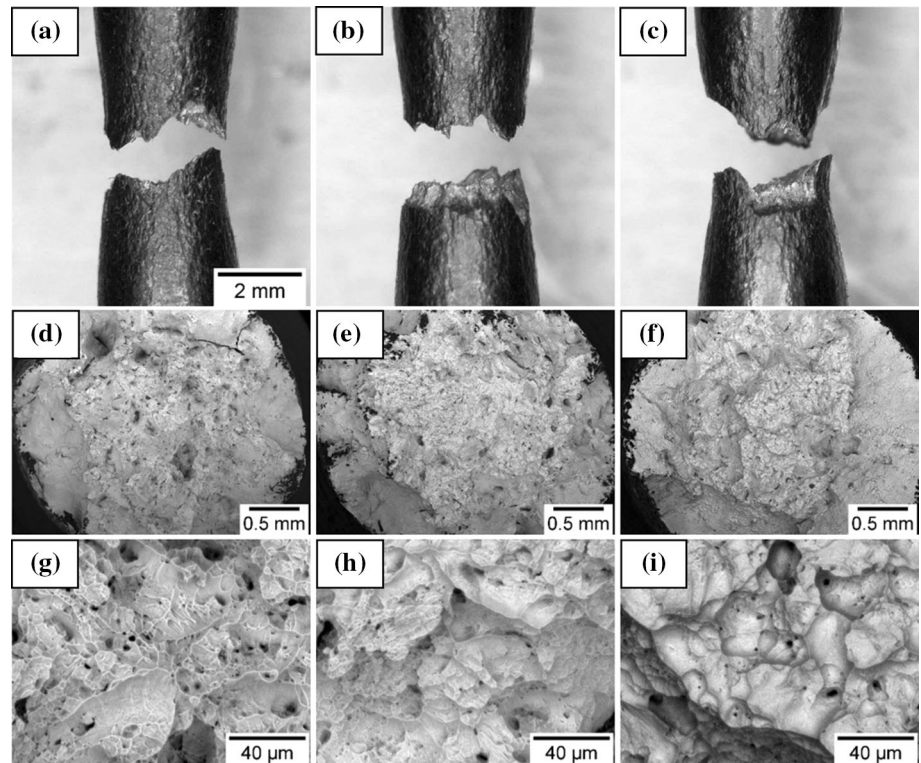

Table 4 The best elastic admissible strain (EAS) obtained for each alloy/condition

Alloy	Condition	EAS % (best)
Ti-23Nb-2.0Fe-10Zr	WQ	1.09
	Aged	1.14
Ti-27Nb-1.5Fe-10Zr	WQ	0.95
	Aged	1.06
Ti-31Nb-1.0Fe-10Zr	WQ	0.89
	Aged	0.93

other hand, early plastic instabilities among aged samples could limit their use depending on the target structural application's strain requirements.

Overall, the alloys presented here are promising candidates to be used in the biomedical field. Upon quenching or aging, they achieved elastic admissible strains close to 1 (Table 4), suitable for structural materials in the biomedical area [29, 42]. Hardness values are also presented as a reference for future works. We decided to use the pulse-echo modulus values to estimate the elastic admissible strains (EASs) displayed in Table 4 since this technique is more reliable than extrapolations from the stress–strain curves.

A compilation with a few alloys from the Ti-Nb-Fe, Ti-Nb-Zr, and Ti-Nb-Fe-Zr systems, their compositions, mechanical properties, and e/a ratios are shown in Table 5. Concerning alloy design aspects, it seems the success of creating novel quaternary compositions should not be directly associated with the well-known electronic parameters such as the e/a ratio. As shown in Fig. 12, it is impossible to establish a direct correlation between elastic modulus and such parameters. Even for a small e/a ratio range (near 4.20), elastic moduli vary from 55 to 90 GPa. According to Wang et al. 2016, the e/a ratio is not a suitable parameter to predict the elastic modulus and the phase stability of multicomponent Ti-Nb-Zr alloys [43] (Fig. 13).

Since compositions with the same e/a ratio can have different shear elastic constants, an estimation of the elastic constants via computational techniques is needed for each specific alloy, making alloy design more intricate than previously thought [23, 44–46]. The elastic modulus of Ti-23Nb-2Fe was reduced by approx. 32% with Zr additions, going from 95 to 72 GPa. According to DFT calculations, only 12% of such reduction can be attributed to structural changes in the β-phase; therefore, the decline may be majorly linked with the ω suppression in Zr presence.

Table 5 Compilation of the mechanical properties of ST-WQ alloys from the literature

Id*	Composition (wt. %)	Ys (MPa)	E (GPa)	EAS	e/a	References
1	Ti-13Nb-13Zr	345	66	0.52	4.077	[47]
2	Ti-34Nb-25Zr	810	62	1.31	4.245	[29]
3	Ti-12Nb-5Fe	740	90	0.82	4.250	[48]
4	Ti-30Nb-3Fe	650	81	0.80	4.303	[10]
5	Ti-19Nb-2.5Fe	672	90	0.75	4.203	[26]
6	Ti-23Nb-2.0Fe	604	95	0.64	4.211	[26]
7	Ti-28Nb-13Zr-0.5Fe	780	58	1.34	4.201	[11]
8	Ti-10Nb-19Zr-1Fe	624	59	1.06	4.100	[12]
9	Ti-32Nb-6Zr-1.5Fe	1038	62	1.67	4.266	[13]
10	Ti-19Nb-10Zr-2.5Fe	1027	69	1.49	4.214	[14]
11	Ti-35Nb-7Zr-5Ta	530	55	0.96	4.255	[49]
12	Ti-23Nb-10Zr-2.0Fe	782	72	1.09	4.223	This work

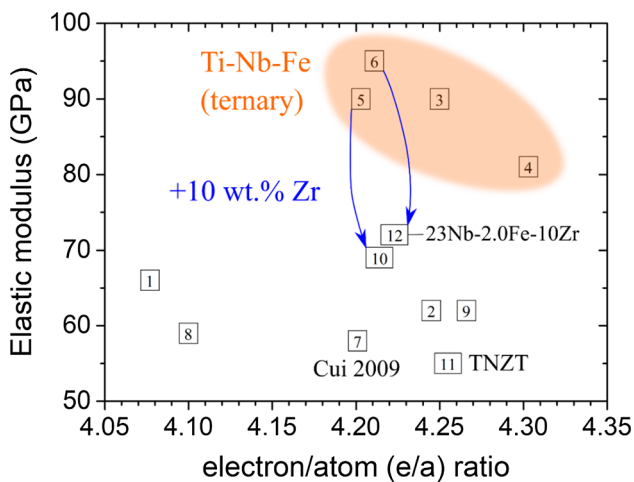*Identification matching Fig. 10

Figure 13 Elastic modulus vs. *e/a* ratio. There is no apparent correlation between these data points; the diagram only explicit the reduction of the elastic modulus with 10 wt.% Zr addition.

Conclusions

We have confirmed there are good candidates among the Ti-Nb-Fe-Zr alloys in the biomedical field. In summary, Zr additions seem crucial to hinder the ω-phase formation and achieve a relatively low elastic modulus among Ti-Nb-Fe-Zr alloys. This hypothesis is supported by DFT calculations and several experimental observations presented through this study, such as the ones highlighted below:

- Semiempirical electronic parameters such as the e/a ratio could not predict the behavior of novel Ti-Nb-Fe and Ti-Nb-Fe-Zr compositions concerning either their elastic modulus or their phase stability.

- Based on the electronic analysis of the β-phase performed via DFT, it is not the magnitude of electronic charge density differences ($\Delta\rho$) that define the elastic properties in this system, but rather its localization and orientation. Charge density differences play an essential role in lattice distortions, thus influencing phase stability.

- Overall, the behavior of Fe-rich alloys diverges from the Nb-rich ones. Fe enables higher mechanical strength but unfortunately leads to a relatively higher elastic modulus.

- A good compromise between strength and modulus is obtained for Ti-23Nb-2.0Fe-10Zr, which presented an elastic admissible strain of 1.14 after aging.

- Zr additions provide an excellent counter-measure to the elastic modulus increase due to Fe presence, operating on two fronts: (1) reducing the elastic modulus of the β matrix and (2) increasing the ω-phase formation energy relative to β.

Declarations

Conflict of interest The authors declare that there is no conflict of interest.

References

[1] Marvel CJ, Sabol JC, Pasang T et al (2017) Improving the mechanical properties of the fusion zone in electron-beam welded Ti-5Al-5Mo-5V-3Cr Alloys. Metall Mater Trans A 48:1921–1930. https://doi.org/10.1007/s11661-017-3968-2

[2] Kolli R, Devaraj A (2018) A review of metastable beta titanium alloys. Metals (Basel) 8:506. https://doi.org/10.3390/met8070506

[3] Devaraj A, Joshi VV, Srivastava A et al (2016) A low-cost hierarchical nanostructured beta-titanium alloy with high strength. Nat Commun 7:11176. https://doi.org/10.1038/ncomms11176

[4] Franti GW, Williams JC, Aaronson HI (1978) A survey of eutectoid decomposition in ten Ti-X systems. Metall Trans A 9:1641–1649. https://doi.org/10.1007/BF02661947

[5] Lee HJ, Aaronson HI (1988) Eutectoid decomposition mechanisms in hypoeutectoid Ti-X alloys. J Mater Sci 23:150–160. https://doi.org/10.1007/BF01174047

[6] Nag S, Banerjee R, Fraser HL (2005) Microstructural evolution and strengthening mechanisms in Ti-Nb-Zr-Ta, Ti-Mo-Zr-Fe and Ti-15Mo biocompatible alloys. Mater Sci Eng C 25:357–362. https://doi.org/10.1016/j.msec.2004.12.013

[7] ASTM International (2013) Standard Specification for Wrought Titanium-12Molybdenum-6Zirconium-2Iron Alloy for Surgical Implant (UNS R58120). https://doi.org/10.1520/F1813-13.2

[8] Lee CM, Ho WF, Ju CP, Chern Lin JH (2002) Structure and properties of Titanium-25 Niobium-x iron alloys. J Mater Sci Mater Med 13:695–700

[9] Hsu H-C, Hsu S-K, Wu S-C et al (2010) Structure and mechanical properties of as-cast Ti–5Nb–xFe alloys. Mater Charact 61:851–858. https://doi.org/10.1016/j.matchar.2010.05.003

[10] Lopes ÉSN, Salvador CAF, Andrade DR et al (2016) Microstructure, mechanical properties, and electrochemical behavior of Ti-Nb-Fe alloys applied as biomaterials. Metall Mater Trans A 47:3213–3226. https://doi.org/10.1007/s11661-016-3411-0

[11] Cui WF, Guo AH (2009) Microstructures and properties of biomedical TiNbZrFe β-titanium alloy under aging conditions. Mater Sci Eng A 527:258–262. https://doi.org/10.1016/j.msea.2009.08.057

[12] Xue P, Li Y, Li K et al (2015) Superelasticity, corrosion resistance and biocompatibility of the Ti-19Zr-10Nb-1Fe alloy. Mater Sci Eng C 50:179–186. https://doi.org/10.1016/j.msec.2015.02.004

[13] Nocivin A, Cinca I, Raducanu D et al (2017) Mechanical properties of a Gum-type Ti–Nb–Zr–Fe–O alloy. Int J Miner Metall Mater 24:909–917. https://doi.org/10.1007/s12613-017-1477-3

[14] Dal Bó MR, Salvador CAF, Mello MG et al (2018) The effect of Zr and Sn additions on the microstructure of Ti-Nb-Fe gum metals with high elastic admissible strain. Mater Des 160:1186–1195. https://doi.org/10.1016/j.matdes.2018.10.040

[15] Esteban PG, Ruiz-Navas EM, Gordo E (2010) Influence of Fe content and particle size the on the processing and mechanical properties of low-cost Ti–xFe alloys. Mater Sci Eng A 527:5664–5669. https://doi.org/10.1016/j.msea.2010.05.026

[16] Kent D, Pas S, Zhu S et al (2012) Thermal analysis of precipitation reactions in a Ti–25Nb–3Mo–3Zr–2Sn alloy. Appl Phys A 107:835–841. https://doi.org/10.1007/s00339-012-6778-9

[17] Kresse G, Furthmiiller J (1996) Efficiency of ab-initio total energy calculations for metals and semiconductors using a plane-wave basis set av *. Comput Mater Sci 6:15–50

[18] Van De Walle A, Tiwary P, De Jong M et al (2013) Efficient stochastic generation of special quasirandom structures. Calphad 42:13–18. https://doi.org/10.1016/j.calphad.2013.06.006

[19] Von Pezold J, Dick A, Friák M, Neugebauer J (2010) Generation and performance of special quasirandom structures for studying the elastic properties of random alloys: Application to Al-Ti. Phys Rev B-Condens Matter Mater Phys 81:1–7. https://doi.org/10.1103/PhysRevB.81.094203

[20] Gaillac R, Pullumbi P, Coudert FX (2016) ELATE: An open-source online application for analysis and visualization of elastic tensors. J Phys Condens Matter. https://doi.org/10.1088/0953-8984/28/27/275201

[21] Momma K, Izumi F (2008) VESTA: A three-dimensional visualization system for electronic and structural analysis. J Appl Crystallogr 41:653–658. https://doi.org/10.1107/S0021889808012016

[22] Todd R, Armstrong D (2006) Gum metal and related alloys. In: Encyclopedia of materials: science and technology. Elsevier, Amsterdam, pp 1–4. https://doi.org/10.1016/B978-0-12-803581-8.11538-3

[23] Saito T, Furuta T, Hwang J-H et al (2003) Multifunctional alloys obtained via a dislocation-free plastic deformation mechanism. Science 300:464–467. https://doi.org/10.1126/science.1081957

[24] Cotton JD, Briggs RD, Boyer RR et al (2015) State of the art in beta titanium alloys for airframe applications. JOM 67:1281–1303. https://doi.org/10.1007/s11837-015-1442-4

[25] da Costa FHFH, Salvador CAFCAF, de Mello MGMG, Caram R (2016) Alpha phase precipitation in Ti-30Nb-1Fe alloys–phase transformations in continuous heating and aging heat treatments. Mater Sci Eng A 677:222–229. https://doi.org/10.1016/j.msea.2016.09.023

[26] Salvador CAFF, Lopes ESNN, Caram R et al (2017) Solute lean Ti-Nb-Fe alloys: an exploratory study. J Mech Behav Biomed Mater 65:761–769. https://doi.org/10.1016/j.jmbbm.2016.09.024

[27] Banerjee D, Williams JC (2013) Perspectives on titanium science and technology. Acta Mater 61:844–879. https://doi.org/10.1016/j.actamat.2012.10.043

[28] Salvador CAF, Opini VC, Lopes ESN, Caram R (2017) Microstructure evolution of Ti–30Nb–(4Sn) alloys during classical and step-quench aging heat treatments. Mater Sci Technol 33:400–407. https://doi.org/10.1080/02670836.2016.1216030

[29] Ozan S, Lin J, Li Y et al (2015) Development of Ti–Nb–Zr alloys with high elastic admissible strain for temporary orthopedic devices. Acta Biomater 20:176–187. https://doi.org/10.1016/j.actbio.2015.03.023

[30] Min XH, Emura S, Zhang L, Tsuzaki K (2008) Effect of Fe and Zr additions on ω phase formation in β-type Ti–Mo alloys. Mater Sci Eng A 497:74–78. https://doi.org/10.1016/j.msea.2008.06.018

[31] Banerjee R, Nag S, Stechschulte J, Fraser HL (2004) Strengthening mechanisms in Ti–Nb–Zr–Ta and Ti–Mo–Zr–Fe orthopaedic alloys. Biomaterials 25:3413–3419. https://doi.org/10.1016/j.biomaterials.2003.10.041

[32] Dobromyslov AV, Elkin VA (2001) Martensitic transformation and metastable beta-phase in binary titanium alloys with d-metals of 4–6 periods. Scr Mater 44:905–910

[33] Fu Y, Xiao W, Wang J et al (2020) Oxygen induced crystal structure transition of martensite in Ti–Nb–Fe alloys. Mater Lett 262:127026. https://doi.org/10.1016/j.matlet.2019.127026

[34] Opini VC, Salvador CAF, Campo KN et al (2016) α phase precipitation and mechanical properties of Nb-modified Ti-5553 alloy. Mater Sci Eng A 670:112–121. https://doi.org/10.1016/j.msea.2016.06.001

[35] Choudhuri D, Zheng Y, Alam T et al (2017) Coupled experimental and computational investigation of omega phase evolution in a high misfit titanium-vanadium alloy. Acta Mater 130:215–228. https://doi.org/10.1016/j.actamat.2017.03.047

[36] Li M, Min X (2020) Origin of ω-phase formation in metastable β-type Ti-Mo alloys: cluster structure and stacking fault. Sci Rep 10:8664. https://doi.org/10.1038/s41598-020-65254-z

[37] Withey EA, Minor AM, Chrzan DC et al (2010) The deformation of gum metal through in situ compression of nanopillars. Acta Mater 58:2652–2665. https://doi.org/10.1016/j.actamat.2009.12.052

[38] Gutierrez-Urrutia I, Li C-L, Emura S et al (2016) Study of {332}<113> twinning in a multilayered Ti-10Mo-xFe (x = 1–3) alloy by ECCI and EBSD. Sci Technol Adv Mater 17:220–228. https://doi.org/10.1080/14686996.2016.1177439

[39] Gorsse S, Hutchinson C, Gouné M, Banerjee R (2017) Additive manufacturing of metals: a brief review of the characteristic microstructures and properties of steels, Ti-6Al-4V and high-entropy alloys. Sci Technol Adv Mater 18:584–610. https://doi.org/10.1080/14686996.2017.1361305

[40] Van Stone RH, Low JR, Shannon JL (1978) Investigation of the fracture mechanism of Ti-5Al-2.5 Sn at cryogenic temperatures. Metall Trans A 9:539–552

[41] Salvador CAF, Opini VC, Mello MG, Caram R (2018) Effects of double-aging heat-treatments on the microstructure and mechanical behavior of an Nb-modified Ti-5553 alloy. Mater Sci Eng A 743:716–725. https://doi.org/10.1016/j.msea.2018.11.086

[42] Biesiekierski A, Lin J, Li Y et al (2016) Investigations into Ti–(Nb, Ta)–Fe alloys for biomedical applications. Acta Biomater 32:336–347. https://doi.org/10.1016/j.actbio.2015.12.010

[43] Wang X, Zhang L, Guo Z et al (2016) Study of low-modulus biomedical β Ti–Nb–Zr alloys based on single-crystal elastic constants modeling. J Mech Behav Biomed Mater 62:310–318. https://doi.org/10.1016/j.jmbbm.2016.04.040

[44] Talling RJ, Dashwood RJ, Jackson M, Dye D (2009) Compositional variability in gum metal. Scr Mater 60:1000–1003. https://doi.org/10.1016/j.scriptamat.2009.02.044

[45] Abdel-Hady M, Hinoshita K, Morinaga M (2006) General approach to phase stability and elastic properties of β-type Ti-alloys using electronic parameters. Scr Mater 55:477–480. https://doi.org/10.1016/j.scriptamat.2006.04.022

[46] Abdel-Hady M, Fuwa H, Hinoshita K et al (2007) Phase stability change with Zr content in β-type Ti–Nb alloys. Scr Mater 57:1000–1003. https://doi.org/10.1016/j.scriptamat.2007.08.003

[47] Majumdar P, Singh SB, Chakraborty M (2011) The role of heat treatment on microstructure and mechanical properties of Ti–13Zr–13Nb alloy for biomedical load bearing

applications. J Mech Behav Biomed Mater 4:1132–1144. https://doi.org/10.1016/j.jmbbm.2011.03.023

[48] Biesiekierski A, Lin J, Li Y et al (2016) Investigations into Ti-(Nb, Ta)-Fe alloys for biomedical applications. Acta Biomater 32:336–347. https://doi.org/10.1016/j.actbio.2015.12.010

[49] Gepreel MA, Niinomi M, Abdel-Hady Gepreel M et al (2013) Biocompatibility of Ti-alloys for long-term implantation. J Mech Behav Biomed Mater 20:407–415. https://doi.org/10.1016/j.jmbbm.2012.11.014